ACS OMEGA

Open Access

http://pubs.acs.org/journal/acsodf

Article

Stable and Highly Efficient Photocatalysis with Two-Dimensional Organic–Inorganic Hybrid Perovskites

Mengke Wang, Xi Zhang, Lei Liu, Xiaoyu Zhang, Jiahe Yan, Weihua Jin, Peng Zhang, and Jun Wang*

Cite This: *ACS Omega* 2024, 9, 3931−3941

Read Online

ACCESS | Metrics & More | Article Recommendations | Supporting Information

ABSTRACT: Two-dimensional organic−inorganic hybrid perovskites (OIHPs) have excellent photoelectric properties, such as high charge mobility and a high optical absorption coefficient, which have attracted enormous attention in the field of optoelectronic devices and photochemistry. However, the stability of 2D OIHPs in solution is deficient. In particular, the lack of stability in polar solutions hinders their application in photochemistry. In this work, $(iso\text{-}BA)_2PbI_4$ was used as a model to explore the three possibilities of the stable existence of a 2D perovskite in aqueous solution. And two of these systems that stabilize the presence of $(iso\text{-}BA)_2PbI_4$ were further investigated through electrochemical testing. Moreover, $(iso\text{-}BA)_2PbI_4$ 2D hybrid perovskites exhibited an outstanding degradation rate. The chiral perovskite $(R/S\text{-}MBA)_2PbI_4$ is able to degrade a 30 mg/L methyl orange solution completely within 5 min, making it one of the fastest catalysts for this particular organic reaction. Further, based on the electron spin resonance test, a degradation mechanism by the halide perovskite was proposed. Based on the great catalytic performance as well as good reusability and stability, $(R/S\text{-}MBA)_2PbI_4$ perovskites are expected to be a new generation of catalysts, making a great impact on the application of asymmetrically catalyzed photoreactions.

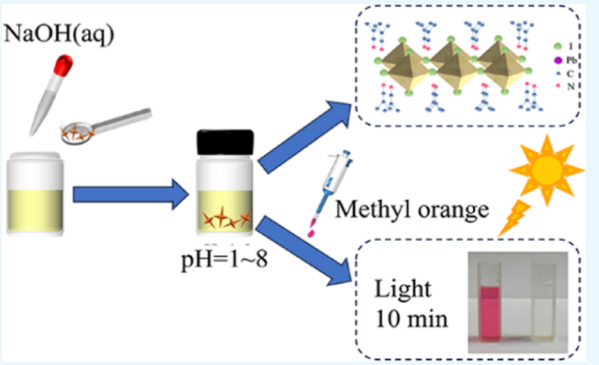

1. INTRODUCTION

Nowadays, the semiconductor-based light reaction, as a green and efficient oxidation technology, is the most promising use of renewable solar energy.[1,2] Over the past few decades, a wide variety of catalysts for photoreactions have been reported, mainly including metal oxides (TiO_2, SnO_2, and ZnO) and metal sulfides (CdS and PbS).[3−5] However, these photocatalysts possess drawbacks of rapid carrier recombination, a smaller light absorption range, and limited stability, limiting large-scale commercial applications.[6] Therefore, the development of new semiconductor photocatalysts with enhanced photocatalytic activity and energy conversion efficiency is of great importance. Recently, 2D perovskites as increasingly promising semiconductor materials have received widespread attention in the research field of optoelectronic devices and photocatalysis, which is attributed to their outstanding optical and electrical properties,[7,8] such as tunable optical band gaps,[9] great charge mobilities,[10] high absorption coefficients,[11] long charge carrier lifetimes, and high photoluminescence (PL) quantum yields.[12,13] To date, hundreds of perovskite-based photocatalysts have been reported with some achieving high photocatalytic efficiency.[14] Thus, perovskite-based photocatalytic materials are promising for practical applications.

The inferior stability and highly ionic character of 3D perovskites compel researchers to focus on low-dimensional perovskites (i.e, 2D perovskites).[15] Two-dimensional perovskites are generally described by the formula $(A')_m(A)_{n-1}B_nX_{3n+1}$, where A′ can be either a monovalent (m = 2) or a bivalent (m = 1) cation, forming a double or single layer of connected inorganic $(A)_{n-1}B_nX_{3n+1}$ two-dimensional sheet, respectively, where n can be regarded as the thickness of the inorganic layer.[16,17] The photoelectric properties of two-dimensional perovskites, such as the band gap and exciton binding energy, are highly dependent on the degree of quantum confinement, which is primarily determined by the thickness of the inorganic layer.[18,19] Specifically, the thickness of the inorganic layer increases with the increase of n values, thus leading to the decrease of the quantum constraint, resulting in a large and tunable reduction of the optical band gap and the tailoring of electrical properties.[20−22]

The reported halide perovskite photocatalysts (HPPs) are generally classified as Pb-based organic−inorganic hybrid perovskites (OIHPs) ($MAPbI_3$, $FAPbI_3$, $MAFAPbI_3$, and $MAFACsPbI_3$), all inorganic perovskites ($CsPbI_3$ and $CsPbBr_3$), lead-free perovskites ($CsSnI_3$, $Cs_2BiAgBr_6$, and $AgBi_2I_7$), and Ruddlesden−Popper layered perovskites. In-

Received: October 23, 2023
Revised: December 16, 2023
Accepted: December 25, 2023
Published: January 8, 2024

organic halide perovskite quantum dots (IHPQDs) have attracted much attention due to their ultrahigh PL quantum yield,[23] continuous absorption in the visible range,[24,25] tunable band gap,[26] and good feasibility of chemical synthesis.[27] Besides, inorganic halide perovskite carbon quantum dots (IHPCQDs) intrinsically have a larger surface area, and the energy levels can be adjusted by tuning the size to further regulate the electron transport.[28,29] Second, CQDs can form a uniform colloidal solution in many organic solvents on account of their high dispersity as well as maintain heterogeneous catalytic properties, including recyclability and separability. However, the poor stability of PQDs in air or water solutions is still a huge challenge to its widespread application.[30]

Lead-free perovskites are the perovskites in which the Pb^{2+} ion is replaced by Sn^{2+}, Ge^{2+}, Mg^{2+}, Mn^{2+}, or other divalent metal cations.[31] Sn-based lead-free perovskites have been intensively researched because the radius of Sn^{2+} (1.35 Å) is similar to that of Pb^{2+} (1.49 Å). Comparing with lead-based perovskites, Sn-based perovskites not only are nontoxic but also possess excellent properties, such as a narrow band gap and high carrier mobility. Unfortunately, the issue of stability badly hinders its application since Sn^{2+} is easily oxidized to Sn^{4+} under ambient conditions.[32,33] Despite the advantageous optoelectronic properties, the Ruddlesden−Popper layered perovskites suffer from severe instability when exposed to water, highly polar solvents, oxygen, light, and heat. Even though some perovskites have achieved a high photocatalytic efficiency, their application in large-scale commercialization is relatively limited. The challenge of large-scale applications derives from two main limitations: lack of chemical stability in polar solvents and surface vulnerability to chemical transformation in solution.[34,35] Hence, the investigation on the stability of 2D OIHPs in polar solutions is the primary issue before the study on its catalytic properties.[36]

Herein, $(iso\text{-}BA)_2PbI_4$ was synthesized by the KI solution method, and its stability was evaluated under three conditions, wherein the as-prepared perovskite remained stable in a wide pH range of 1−8. And its electrochemical stability was further confirmed by electrochemical and X-ray photoelectron spectroscopy (XPS) characterizations. And $(iso\text{-}BA)_2PbI_4$ emerges as having excellent capability in photocatalytic degradation of organic dyes, which can efficiently degrade methyl orange dye within 10 min without the loss of stability. Moreover, the catalytic performance of $(R/S\text{-}MBA)_2PbI_4$ was found to be superior to that of $(iso\text{-}BA)_2PbI_4$, $(BA)_2PbI_4$, and $(PEA)_2PbI_4$ organo-amine ligands, which was confirmed by both the organic dye degradation experiment and electrochemical impedance spectroscopy (EIS). It is worth mentioning that the chiral perovskite $(R/S\text{-}MBA)_2PbI_4$ achieved near-complete degradation of a 30 mg/L methyl orange solution in just 5 min, which is one of the most efficient catalysts to our knowledge for methyl orange degradation until now, having significant implications for the exploration of asymmetric catalysis research and development of high-performance catalysts.

2. MATERIALS AND METHODS

2.1. Materials. The chemicals were purchased from different companies as follows: lead(II) iodide (PbI_2, 99%, Sigma-Aldrich), potassium iodide (KI, 99%, Macklin), isobutylamine ($C_4H_{11}N$, 99.5%, Aladdin), hypophosphorous acid (H_3PO_2, 50 wt % in H_2O, Macklin), *n*-butylamine ($C_4H_{11}N$, 99%, Aladdin), *β*-phenylethylamine ($C_8H_{11}N$, 98%, Aladdin), (*R*)-(+)-*α*-methylbenzylamine ($C_8H_{11}N$, 99%, Macklin), (*S*)-(−)-*α*-methylbenzylamine ($C_8H_{11}N$, 99%, Aladdin), sodium hydroxide (NaOH, 98%, Macklin), methyl orange ($C_{14}H_{14}N_3NaO_3S$, AR, Tianjin Tianxin Fine Chemical Development Center), congo red ($C_{32}H_{22}N_6Na_2O_6S_2$, Tianjin Institute of Chemical Reagents), direct black 19 ($C_{34}H_{27}N_{13}Na_2O_7S_2$, Maya Reagent), sulforhodamine-B ($C_{27}H_{29}N_2NaO_7S_2$, 85%, Macklin), ethylenediamine tetraacetic acid ($C_{10}H_{16}N_2O_8$, AR, Damao chemical reagent), *p*-quinone ($C_6H_4O_2$, 99%, Maya Reagent), silver nitrate ($AgNO_3$, AR, Damao chemical reagent), and isopropyl alcohol (C_3H_8O, AR, Tian in Fuyu Fine Chemical Co., Ltd.). All chemical reagents were used as received without further purification, and deionized (DI) water (>18 MΩ) was used throughout the experiments.

2.2. Preparation of $(iso\text{-}BA)_2PbI_4$. KI powder (6 g, 36 mmol) was dissolved in 9 mL of DI water. Then, 0.1383 g of PbI_2 was dissolved in KI solution and stirred continuously until it was clarified. The iso-BA (180 μL) in a separate vial was first neutralized by adding 500 μL of H_3PO_2, and then, the obtained protonated solution was added dropwise to the KI solution with stirring. The mixed solution was subsequently set overnight without stirring to yield plate crystals of orange color, which was collected by suction filtration and dried for 4 h at 60 °C in a vacuum oven before use.

2.3. Preparation of $(BA)_2PbI_4$. PbI_2 powder (138.3 mg, 0.3 mmol) was first added to 9 mL of KI solution that was prepared under the above procedure. In a separate vial, 420 mL of BA was neutralized and protonated by the reaction with 1500 μL of H_3PO_2 and then added dropwise to the previous solution with stirring. The mixed solution was then allowed to precipitate overnight without stirring to produce yellow plate-like crystals, which were further collected by suction filtration and dried in a vacuum oven at 60 °C for 4 h prior to use.

2.4. Preparation of $(PEA)_2PbI_4$. A solution of KI prepared by dissolving 4 g of KI (24 mmol) in 6 mL of DI water was mixed with PbI_2 powder (46.1 mg, 0.1 mmol) under stirring until clear. In a separate vial, 25 μL (0.2 mmol) of PEA was neutralized by adding 500 μL of H_3PO_2, and then, the protonated PEA solution was added dropwise to the previous solution with stirring. After leaving standing overnight without stirring, orange plate-like crystals were obtained, collected by suction filtration, and then dried subsequently in a vacuum oven at 60 °C for 4 h before use.

2.5. Preparation of $(R/S\text{-}MBA)_2PbI_4$. The KI solution was prepared by dissolving 4 g of KI (24 mmol) in 6 mL of DI water, which was further mixed with PbI_2 powder (92.2 mg, 0.2 mmol) until clear. In the separated vials, 660 μL of H_3PO_2 and 256 μL (1.4 mmol) of *R*/*S*-MBA were first mixed, and the obtained protonated *R*/*S*-MBA solution was added to the previously acquired solution dropwise with stirring. After being left standing without agitation overnight, orange needle-like crystals were yielded, which were further collected by suction filtration and then dried in a vacuum oven at 60 °C for 4 h before use.

2.6. Characterization. The powder X-ray diffraction (XRD) patterns of the samples were recorded on a powder X-ray diffractometer (Empyrean, PANalytical B.V.) using Cu $K\alpha_1$ radiation. The UV−vis absorption spectra were obtained by a UV−vis spectrophotometer (UV-5200PC, ShangHai Metash Instruments Co., Ltd.). Diffuse reflection spectra were acquired with a UV−vis spectrophotometer (Lambda 750, PerkinElmer). The PL measurements were performed using a fluorescence spectrometer (Fluoromax-4, HORIBA)

https://doi.org/10.1021/acsomega.3c08356
ACS Omega 2024, 9, 3931−3941

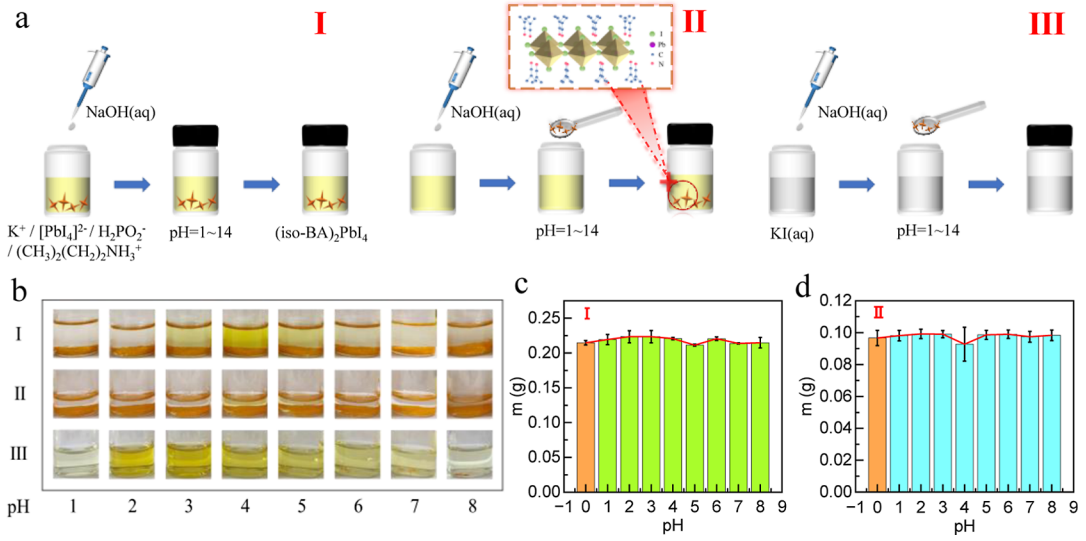

Figure 1. Study on the stability of the 2D halide perovskite. (a) Schematic illustration of the exploration of the stability of $(iso\text{-}BA)_2PbI_4$. [Inset: crystal structure of $(iso\text{-}BA)_2PbI_4$]. The three schemes are denoted as schemes I, II, and III, respectively. (b) Optical photograph of the perovskite present at pH = 1−8 (in schemes I, II, and III). (c) Mass distribution of the sample at pH = 1−8 in Scheme I. (d) Mass distribution of the samples at pH = 1−8 in Scheme II.

equipped with a monochromatized Xe lamp as the excitation source. The morphology and microstructures of the samples were investigated by using a scanning electron microscopy (SEM) system (Hitachi SU-8010) with a 25 kV acceleration voltage. The high-resolution transmission electron microscopy (HR-TEM) images were collected on an FEI Tal os F200X transmission electron microscope with an accelerating voltage of 200 kV. The electron spin resonance (ESR) spectra of the radical spin-trapped by DMPO were detected on a Bruker model A300-10/12 spectrometer under visible light irradiation. The XPS measurements of the samples were conducted on an ESCALAB 250Xi X-ray photoelectron spectrometer (Thermo Fischer, America) equipped with an A1 Kα X-ray source. The shift of the binding energy due to relative surface charging was corrected using the C 1s level at 284.8 eV as an internal standard. An X-ray photoelectron spectrometer (Thermo Fischer, ESCALAB 250Xi, USA) was used for UPS testing. Here, the vacuum of the analyzing chamber is about 2×10^{-8} mbar, the excitation source is HeI UV, the excitation source energy is 21.22 eV, the working voltage is 12.5 kV, the filament current is 16 mA, and the signal accumulation is carried out for 10 cycles.

2.7. Sample Stability Test. Rather than being further separated by suction filtration, the yielded perovskite crystals were kept in the mother liquor to evaluate the stability, which was subsequently adjusted to an integer pH value of 1−14, respectively. In the second way, a certain amount of perovskite samples (0.10 g) was taken out to explore the stability in filtrates of pH 1−14 (adjusted with sodium hydroxide). In the third method, 100 mg perovskite samples were added into potassium iodide solution with an integer pH value of 1−14 to examine the stability.

2.8. Electrochemical Measurement. Electrochemical measurements were performed on a CHI600E electrochemical workstation using a three-electrode system. The samples were loaded on a glassy carbon electrode using silver glue as the medium to function as a working electrode. And a Ag/AgCl electrode (3.5 M KCl) and a Pt sheet were used as the reference electrode and counter electrode, respectively. The electrolyte was the stock solution of different pH values (1−14), which is adjusted by adding an appropriate amount of sodium hydroxide. All pH measurements were done using a PHS-3E INESA instrument. The cyclic voltammetry (CV) curves were measured at a scan rate of 50 mV/s. EIS measurements were carried out over a frequency range of 0.1−100,000 Hz at a scan rate of 50 mV/s.

2.9. Photocatalytic Degradation of the Dyes. The photocatalytic activities were investigated through the degradation of the methyl orange (MO), congo red, direct black 19, and sulforhodamine-B. Typically, the quantitative photocatalyst was dispersed in the aqueous solution of dye (30 mg/L) for 30 min to reach equilibrium. Afterward, the suspension was irradiated with visible light by fluorescent tubes (21 V 150 W) with a halogen cold light source, and 4 mL of the dye solution was removed at 2 min intervals during the irradiation. And the concentration of the remaining dye was determined by measuring the absorption using a UV−vis spectrophotometer (UV-5200PC, ShangHai Metash Instruments Co., Ltd.). The removal rate of the target organic dyes can be calculated according to the equation

$$D = (A_0 - A_t)/A_0 \times 100\%$$

In which, A_t is the absorbance of the organic dye measured at time t and A_0 is the initial absorbance of the organic dye before irradiation.

3. RESULTS AND DISCUSSION

3.1. Stable Existence of the 2D Halide Perovskite. The synthesis of 2D halide perovskites is detailed in the Materials and Methods section and denoted as $(iso\text{-}BA)_2PbI_4$. And Figure 1a schematically demonstrates the three methods to explore the stability of 2D organic and inorganic hybrid halide perovskites, which are represented as Scheme I, Scheme II, and Scheme III, respectively. In Scheme I, the yielded perovskite $(iso\text{-}BA)_2PbI_4$ did not undergo separation of suction filtration yet was kept in the solution that produced it. Then, the pH of the solution was adjusted to an integer value of 1−14 by adding an appropriate amount of NaOH to explore the

https://doi.org/10.1021/acsomega.3c08356
ACS Omega 2024, 9, 3931−3941

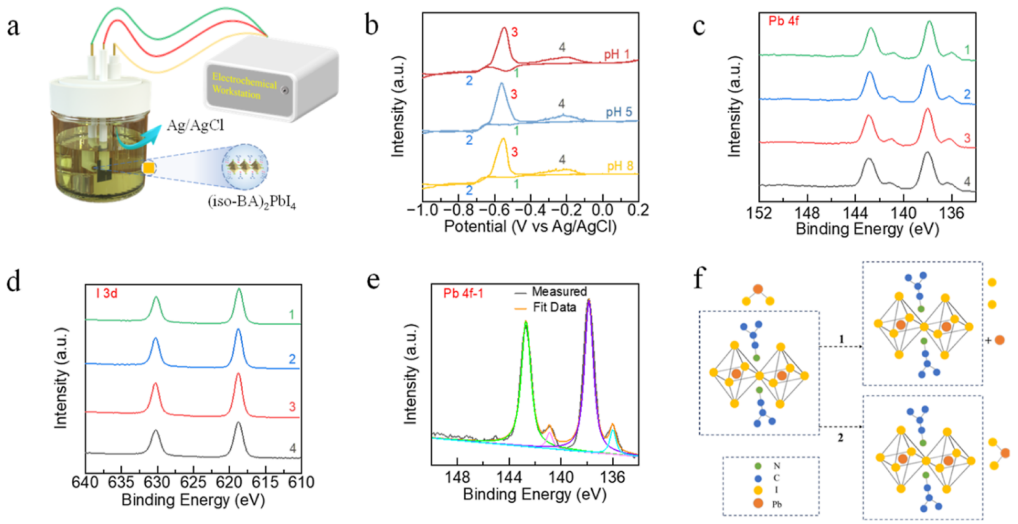

Figure 2. Electrochemical and XPS investigation on the stability of the 2D halide perovskite. (a) Schematic diagram of the electrochemical test using a three-electrode system. (b) Cyclic voltammogram of $(iso\text{-}BA)_2PbI_4$ recorded at pH = 1, 5, and 8. The four redox peaks are labeled as peak 1, peak 2, peak 3, and peak 4. X-ray photoelectron spectra of Pb 4f (c) and I 3d (d) core levels for $(iso\text{-}BA)_2PbI_4$ at peak 1, peak 2, peak 3, and peak 4. The energy position of each spectrum is calibrated using the C 1s peak at 284.8 eV as a reference. (e) XPS analysis of Pb 4f of $(iso\text{-}BA)_2PbI_4$ at peak 1. (f) Crystal structure of $(iso\text{-}BA)_2PbI_4$ undergoes electrochemical processes at various applied potentials. The middle panel represents $(iso\text{-}BA)_2PbI_4$, whereas the right panels represent its oxidation and reduction processes, respectively.

stability of $(iso\text{-}BA)_2PbI_4$ under conditions of acidity/alkalinity (Figure S1). Scheme II involves adding a certain amount (0.10 g) of the perovskite sample that was separated and dried and examining its stability in the filtrate of pH 1−14 (Figure S2). Since the K^+ ion cannot be eliminated and the role of KI cannot be ignored,[7] 0.10 g of the dried sample was put into potassium iodide solution (4 mol/L) with pH values of 1−14 (Scheme III) to investigate the stability (Figure S3).

As illustrated in Figures 1b and S5, the results indicate that the perovskite can remain stable in the pH range of 1−8 under the conditions of Scheme I and Scheme II. In Scheme III, however, the perovskite dissolves and cannot be stabilized. It is worth noting that the solution appears to be of yellow color when pH = 3−5, with the most prominent color at pH = 4. After the addition of the starch indicator, the solution of pH 3, 4, and 5 turned orange, blue-purple, and purple color (Figure S6), respectively, confirming the existence of iodine. In order to further investigate its stability, we compared the mass of the stabilized perovskite samples with that of the blank samples, and the results are shown in Figure 1c,d. As observed from the mass distribution of different pH values obtained by Scheme I, the lowest mass value that was taken as the mean of 3 trials is found to be 0.2113 g at pH 5, and the decrease in mass is attributed to dissolution in the solution. The difference between its mass and the average mass at different pH values divided by the average mass value was 3.30%. Instead, the lowest mass measured in Scheme II was 0.0966 g; that is 1.22% difference regarding with the average at different pH values (Figure 1d).

In addition, the perovskites from pH 1−8 in Scheme I and Scheme II were collected for comparison after filtration and drying, and the crystal structure of these materials was characterized by XRD. As confirmed by Figure S4a,d, the diffraction results of the synthesized blank sample are consistent with the reported data of $(iso\text{-}BA)_2PbI_4$. And there is no significant difference observed between the characteristic diffraction peaks at pH = 2, 4, 6, 8 and the blank sample, corroborating the good stability of the as-prepared perovskite. In addition, the optical properties of the 2D halide perovskite (Figure S4b,c,e,f) were analyzed through PL and ultraviolet−visible absorption spectroscopy. From the absorption spectrum, the positions of the absorption peaks are basically consistent, and band-to-band transitions and free exciton absorption can also be observed. Here, the short-wavelength absorption can be attributed to band−band transitions, whereas the long-wavelength absorption can be attributed to free excitons. The emission peak of the original sample in Scheme I is situated at 566 nm, while the emission peaks of the samples with various pH values (pH 2, 4, 6, and 8) are found at 567 nm in the PL spectrum. Moreover, the emission peaks of the blank and the sample with pH = 2, 4, 6, and 8 in Scheme II are located at 566, 565, 564, 565, and 566 nm, respectively. Accordingly, there is no significant difference in the emission peak positions of the samples. Overall, the above results indicate that perovskite $(iso\text{-}BA)_2PbI_4$ can remain stable in the original solution from pH 1 to pH 8 (in Scheme I). And it is worth noting that the sample can maintain good stability even after drying and being redissolved by the filtrate in a pH range of 1−8 (in Scheme II). When the solution is alkaline, the substance begins to dissolve and white $Pb(OH)_2$ is formed (Figures S1 and S2).[37] The reaction equation is

$$[PbI_4]^{2-} + 2OH^- = Pb(OH)_2 \downarrow + 4I^-$$

The stable perovskite systems we explore in this paper contain certain amounts of K^+ and Pb^{2+}. Owing to the reinforced ionic bonding formed by the K^+ and Pb^{2+} in solution and the surface iodine ion, the potassium-passivated perovskite in our study shows significantly improved stability, so it can exist stably. To our knowledge, our halide perovskite materials exhibit exceptional stability in the polar solution of various pH values (pH 1−8) under an ambient atmosphere.

To further evaluate the stability theoretically, electrochemical characterization was applied to elucidate the fundamental energetics of the halide perovskites. Voltammetry and impedance spectroscopy can reveal the frontier and excited state orbitals, defect and doped states, density of states,

https://doi.org/10.1021/acsomega.3c08356
ACS Omega 2024, 9, 3931−3941

electron−hole transfer rate, conductivity, dielectric constants, and more.[38] Besides, CV can also be used to evaluate the stability of substances. Therefore, electrochemical tests were performed in a three-electrode system, in which a glassy carbon electrode was coated with $(iso\text{-}BA)_2PbI_4$ with silver gel used as the working electrode, a Ag/AgCl electrode used as the reference electrode, and a platinum sheet used as the counter electrode (Figure 2a). And CV measurements were performed at a scan rate of 50 mV/s in stock solutions with different pH values (1−8) to understand the redox process (Figures S7 and S8). Upon cycling between 0.2 and −1.0 V (vs Ag/AgCl) with 0 V as the starting potential, the following observations were obtained: (i) no obvious oxidation peak appeared between 0 and 0.2 V and two reduction peaks appeared in the reverse scan, one between −0.49 and −0.55 V (peak 1) and another between −0.7 and −0.75 V (peak 2); (ii) When scanning back to 0 V, an oxidation peak between −0.52 and −0.61 V (peak 3) and another oxidation peak between −0.18 and −0.28 V (peak 4) are observed. Four prominent peaks are evident, labeled peaks 1, 2, 3, and 4, respectively, as in Figure 2b. In addition, Tables 1 and S1 summarize the potentials of the four main peaks and the reactions involved in the four main peaks at different pH (pH 1 to pH = 8) conditions. The first oxidation peak (1) is attributed to the oxidation of $H_2PO_2^-$ to $H_2PO_3^-$, while the second reduction peak (4) is attributed to the reduction of $H_2PO_3^-$ to $H_2PO_2^-$. Based on this electrochemical cycling, peaks 2 and 3 shall be assigned to the oxidation of Pb^0 to Pb^{2+} and the reduction of Pb^{2+} back to Pb^0, respectively.

Table 1. Potentials Comparison of Peaks 2 and 3 and the Corresponding Reactions at Different pH Values

pH	2 ($Pb - 2e^- + 2I^- = PbI_2$) (V)	3 ($PbI_2 + 2e^- = Pb + 2I^-$) (V)
pH = 1	−0.725	−0.544
pH = 2	−0.732	−0.532
pH = 3	−0.7	−0.601
pH = 4	−0.749	−0.52
pH = 5	−0.735	−0.557
pH = 6	−0.725	−0.577
pH = 7	−0.738	−0.56
pH = 8	−0.742	−0.558

To elucidate the above redox processes, the CV spectrum of the sample at pH = 3 (Figure S8c) was comprehensively analyzed, and XPS spectra were further investigated. Four samples that were taken at the potential of peaks 1, 2, 3, and 4 underwent full spectrum scan, as shown in Figure S9. Therein, high-resolution spectra of Pb 4f and I 3d are displayed in Figure 2c,d, while the spectra for the other relevant elements are depicted in Figure S12. The peak location of each spectrum was typically calibrated using the C 1s peak at 284.8 eV as a reference (Figure S11).[39] The spectral fitting peaks of Pb 4f and I 3d are given in Figures 2d,e and S10, and the fitted values for each single item are shown in Table 2. In Figure 2d, the sample (peak 1) has two main peaks located at 630.13 and 618.73 eV, which can be assigned to I $3d_{3/2}$ and I $3d_{5/2}$, respectively. As shown in Figure 2d, the peaks located at 140.93 and 136.03 eV correspond to Pb $4f_{5/2}$ and Pb $4f_{7/2}$, respectively, and thus can be identified as metallic Pb^0 species. The Pb 4f peaks of the sample (peak 1) are separately located at 142.73 and 137.83 eV, which are ascribed to Pb^{2+} species from Pb−I bonding in the perovskite.[40] Through the analysis of Pb 4f and I 3d orbitals, it can be found that the band gap energy corresponding to the peak shows no obvious shift after an electrochemical cycle (Figure 2c,d and Table 2), further evidencing the superior stability of $(iso\text{-}BA)_2PbI_4$ in specific aqueous solution. All of the electrochemical redox processes of $(iso\text{-}BA)_2PbI_4$ are summarized in Figure 2f: at a potential of −0.70 V, the PbI_2 present in the system reacts as follows: $Pb - 2e^- + 2I^- = PbI_2$; at a potential of −0.601 V, PbI_2 gains electrons and undergoes a decomposition reaction, resulting in the formation of Pb^0 detrimental byproducts.

Table 2. Comparison of the Fitted Peaks of the Corresponding Pb 4f and I 3d Spectra at Peak 1, Peak 2, Peak 3, and Peak 4

peak	Pb $4f_{5/2}$ (eV)	Pb $4f_{5/2}$ (eV)	Pb $4f_{7/2}$ (eV)	Pb $4f_{7/2}$ (eV)	I $3d_{3/2}$ (eV)	I $3d_{5/2}$ (eV)
1	142.73	140.93	137.83	136.03	630.13	618.73
2	142.84	141.04	137.94	136.14	630.24	618.74
3	142.92	141.12	138.02	136.22	630.22	618.82
4	142.84	141.14	138.04	136.24	630.24	618.74

On the basis of the stable presence of $(iso\text{-}BA)_2PbI_4$, we investigated the stability of $(PEA)_2PbI_4$ in Scheme I and Scheme II. The results are shown in Figures S13−S15. The results indicate that perovskite $(PEA)_2PbI_4$ is stable from pH 1 to 8 in the original solution (as shown in Scheme I). It is noteworthy that the samples remain well stabilized even after drying and redissolving in the filtrate at pH 1 to 8 (see Scheme II).

3.2. Photocatalytic Applications. The application of 2D halide perovskites in photochemical reactions was further investigated via catalytic degradation of dyes under two main conditions for the stable existence of perovskites (Scheme I and Scheme II). To investigate the photocatalytic activities of $(iso\text{-}BA)_2PbI_4$, four classical dyes, methyl orange (MO), congo red (CR), direct black 19 (DB19), and sulforhodamine-B (SRB), were employed as target organics. Considering the influence of dark adsorption conditions, we tested the UV−vis absorption spectra of the sample kept for 30 min in the dark and exposed to light for different periods of time. As shown in Figure S16, the removal rate of methyl orange was 1.42 and 99.91% under the dark and light conditions, respectively, confirming that the main pathway has more adsorption and a higher catalytic effect. The sample was stirred with the dye for 30 min to reach equilibrium of absorption before irradiation with a halogen cold light source, recorded as light 0 min. Figure 3a reveals the UV−visible absorption spectra and optical photographs corresponding to the photocatalytic degradation of methyl orange (30 mg/L) by the unfiltered sample (Scheme I). In addition, 50 mg of $(iso\text{-}BA)_2PbI_4$ and 50 μL of 3 g/L MO solution were added to 5 mL of the filtrate for the photocatalytic reaction, and methyl orange was almost completely degraded within 10 min, as demonstrated in Figure 3d.

Table 3 summarizes the comparative effectiveness of photocatalytic degradation of dye by the substances in the literature and ours, indicating that $(iso\text{-}BA)_2PbI_4$ reveals excellent photocatalyst efficiency on the degradation of MO. Moreover, Figure 3b,e depicts the photocatalytic degradation capacity of our samples for the four selected organic pollutants as present in Scheme I and II. Without filtering, the degradation rates of the four dyes by $(iso\text{-}BA)_2PbI_4$ were 99.3% (MO), 99.6% (SRB), 88.8% (CR) and 34.8% (DB19),

https://doi.org/10.1021/acsomega.3c08356
ACS Omega 2024, 9, 3931−3941

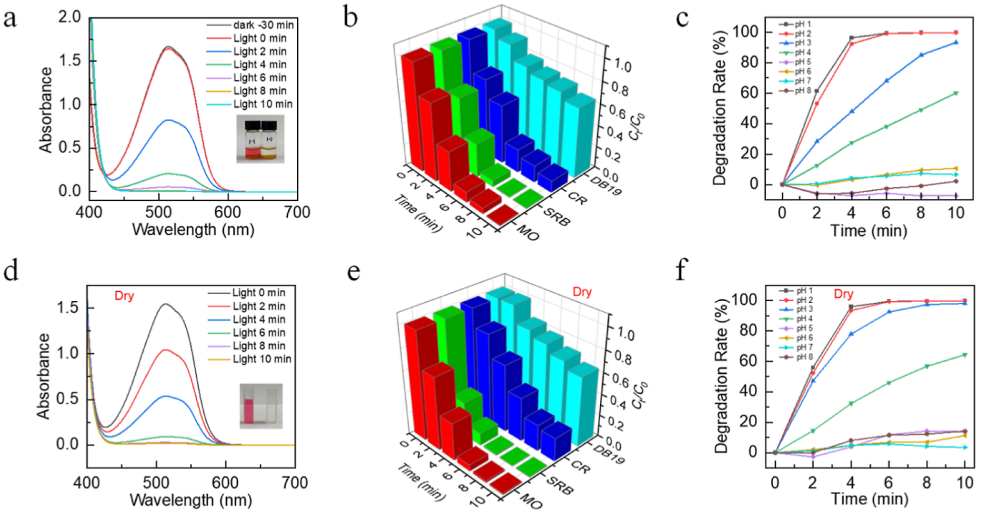

Figure 3. Photocatalytic applications. (a,d) UV−vis spectra at different reaction times during the degradation of MO by $(iso\text{-}BA)_2PbI_4$ in Scheme I (a) and Scheme II (d), respectively. The inset photographs represent the color change of the solution at 0 min of light and 10 min from left to right. The initial concentration of MO was 30 mg/L, and the light source was a halogen lamp. (b,e) Three-dimensional bar chart of C_t/C_0 vs degradation time for different dyes: methyl orange (MO), sulforhodamine-B (SRB), congo red (CR), and direct black 19 (DB19) in Scheme I (b) and in Scheme II (e). (c,f) Degradation rate (%) of $(iso\text{-}BA)_2PbI_4$ on MO vs time at different pH values in Scheme I (c) and in Scheme II (f).

Table 3. Photocatalytic Activity Comparison of $(iso\text{-}BA)_2PbI_4$ and Other Photocatalysts on the Degradation of the Dye

composite	reaction conditions	dye	time	refs
$(iso\text{-}BA)_2PbI_4$	original solution	MO 30 mg/L	10 min	this work
$(R\text{-}MBA)_2PbI_4$	original solution	MO 30 mg/L	5 min	this work
$(S\text{-}MBA)_2PbI_4$	original solution	MO 30 mg/L	5 min	this work
30 wt % Ag−AgI/Bi_3O_4Cl	aqueous solution	MO 20 mg/L	180 min (61%)	42
MM-Fe−Si-PC	40 Mm H_2O_2	MO 20 mg/L	40 min	43
Ag_2Onanoparticle/TiO_2 nanobelt heterostructures	aqueous solution	MO 20 mg/L	35 min (87%)	44
Pt/$Bi_{12}O_{17}C_{l2}$	aqueous solution	MO 10 mg/L	180 min (97%)	45
Ag−AgBrTiO_2	aqueous solution	MO 10 mg/L	110 min (88%)	46
$Cs_2AgBiBr_{6^-}$	aqueous solution	MO 10 mg/L	420 min	47
hollow Co nanoparticle	aqueous solution	MO 100 mg/L	4 min	48
3D N−TiO_{2-x}@MoS_2	aqueous solution	MO 10 mg/L	120 min 91.8%	49
keratin/Ce-MOF	aqueous solution	trypan blue	10 min 98%	50
0.05 M Zn−Mg−Al LTHs/DE(0.05LDE)	aqueous solution	congo red 10 mg/L	96.5% 5 min	51
$CsPbBr_3$	sopropanol solution	methylene blue 0.05 mM	completely disappear 60 min	52

respectively (Figure 3b). And the degradation effect in the condition of Scheme II is depicted in Figure 3e, in which the degradation rates within 10 min were found to be 98.8% (MO), 99.3% (SRB), 78.3% (CR) and 35.4% (DB19) and are almost the same as those of Scheme I. Among them, the catalytic effect of $(iso\text{-}BA)_2PbI_4$ on SRB is shown in Figure S17. Similarly, we also explored the effect of different pH values on the photocatalytic effect under the two stable conditions of Scheme I and Scheme II (Figure 3c,f). Under different pH conditions, the UV−vis absorption spectra of the catalytic process of $(iso\text{-}BA)_2PbI_4$ upon MO are detailed in Figures S18 and S19. It was found that the degradation rate decreases at first and then increases with increasing pH values. And this phenomenon may be ascribed to the massive adsorption of the dye by the catalyst under acidic conditions, making the photocatalytic efficiency enhanced. Although the above adsorption effect is negligible under alkaline conditions, the condition of a high OH^- concentration is conducive to the production of $^{\bullet}OH$, further making the photocatalytic efficiency higher than that in a neutral solution. It can be seen from Figure 5a that hydroxyl radicals are not active species and why the photocatalytic degradation efficiency of the sample at pH = 8 is higher than that under neutral conditions. Additionally, the molecular conformation of methyl orange causes a change in its quinonoid formula, which is unstable and easily broken down at pH = 3.2, whereas methyl orange exists in the azo formula with strong azo bonds and is not easily broken down above pH = 4.4.[41] In wastewater treatment, the removal of the dye may be affected by the presence of a significantly high concentration of salt ions. In this regard, the effect of salt was investigated here by adding various concentrations (from 0.1 to 0.9 M) of chloride salts to the dye solution. As shown in Figure S20, $(iso\text{-}BA)_2PbI_4$ leads to 98.68 and 99.49% dye removal under 0.1 and 0.5 M Cl^- concentrations, respectively. At higher salt concentrations, such as 0.9 M, the removal rate is 99.08%. With increasing salt concentration, the level of methyl orange removal first increased and then decreased. However, the overall effect of salts was negligible.

After the study on the photocatalytic chemical properties of the halide perovskite $(iso\text{-}BA)_2PbI_4$, we further examine the effect of the 2D organo-inorganic hybrid perovskite containing

https://doi.org/10.1021/acsomega.3c08356
ACS Omega 2024, 9, 3931−3941

different organic amine ligands on the photocatalytic performance since OIHPs have tunable band gaps, different optoelectronic properties, and stability due to their organic ligands. The 2D perovskites $(BA)_2PbI_4$, $(PEA)_2PbI_4$, and $(R/S\text{-}MBA)_2PbI_4$ were synthesized by a similar KI solvent method, which is detailed in the Materials and Methods section. Under the same condition of Scheme I, five samples were studied for the degradation of MO (30 mg/L) to evaluate catalytic performance. As shown in Figure 4a, the degradation rates of

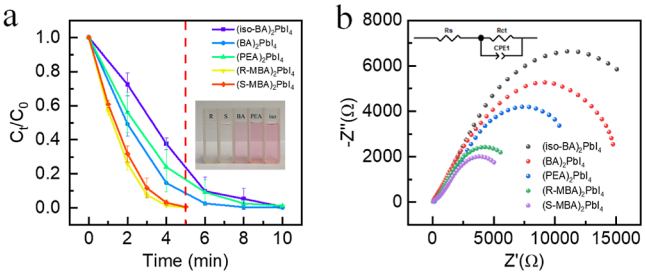

Figure 4. Photocatalytic applications. (a) Removal of MO by photocatalytic processes of $(iso\text{-}BA)_2PbI_4$, $(BA)_2PbI_4$, $(PEA)_2PbI_4$, and $(R/S\text{-}MBA)_2PbI_4$. The inset is the optical photograph of the five sample solutions in the cuvette after 5 min of light exposure. (b) EIS of $(iso\text{-}BA)_2PbI_4$, $(BA)_2PbI_4$, $(PEA)_2PbI_4$, and $(R/S\text{-}MBA)_2PbI_4$. (The inset is the simulated equivalent circuit).

$(R\text{-}MBA)_2PbI_4$ and $(S\text{-}MBA)_2PbI_4$ for MO reached as high as 99.8 and 99.4% within 5 min, respectively, and the degradation performance is also exhibited by the optical photos of the five samples taken at 5 min (the inset). It is obvious that the catalytic effect of chiral perovskites is much higher than those of the other three perovskites (Figure S21). Comparing with the efficiency listed in Table 3, our chiral perovskite $(R/S\text{-}MBA)_2PbI_4$ can be regarded as one of the fastest photocatalysts upon the degradation of MO at present.

EIS was often carried out to understand the charge transfer property of materials.[53] To further evaluate the photocatalytic performance of $(iso\text{-}BA)_2PbI_4$, $(BA)_2PbI_4$, $(PEA)_2PbI_4$, $(R\text{-}MBA)_2PbI_4$, and $(S\text{-}MBA)_2PbI_4$, EIS was conducted (Figure 4b) with an amplitude of 0.1−100,000 Hz, and the equivalent circuit was simulated as shown in the inset. The x-axis intercept of the semicircle is the equivalent resistance of the electrode materials in series, while the diameter of the semicircle could represent the charge transfer resistance. EIS results indicated that the chiral perovskites $(R\text{-}MBA)_2PbI_4$ and $(S\text{-}MBA)_2PbI_4$ possess smaller resistance (R_{ct}) than other perovskites, evidenced by the smaller semicircular arcs (Table 4). And the ion transfer (R_{ct}) values for $(iso\text{-}BA)_2PbI_4$, $(BA)_2PbI_4$, $(PEA)_2PbI_4$, $(R\text{-}MBA)_2PbI_4$, and $(S\text{-}MBA)_2PbI_4$ were found to be 23,662, 17,222, 14,058, 8477, and 7255 Ω, respectively, which evidences that $(R\text{-}MBA)_2PbI_4$ and $(S\text{-}MBA)_2PbI_4$ can transfer charge carriers more efficiently.

Table 4. EIS Spectral Fitted Values of $(iso\text{-}BA)_2PbI_4$, $(BA)_2PbI_4$, $(PEA)_2PbI_4$, $(R\text{-}MBA)_2PbI_4$, and $(S\text{-}MBA)_2PbI_4$

composite	R_s (Ω cm^2)	R_{ct} (Ω cm^2)	R (Ω cm^2)
$(iso\text{-}BA)_2PbI_4$	475.4	23,662	23186.6
$(BA)_2PbI_4$	747.8	17,222	16474.2
$(PEA)_2PbI_4$	877.2	14,058	13180.8
$(R\text{-}MBA)_2PbI_4$	435.9	8477	8041.1
$(S\text{-}MBA)_2PbI_4$	592.1	7225	6632.9

Overall, the EIS results are consistent with those observed by photocatalytic experiments, revealing the great potential of chiral perovskites to become next-generation catalysts. This study not only inspires the design of novel photocatalysts but also provides new insights into the utilization of perovskites in the construction of natural and unnatural compounds with photoactivity.

3.3. Stability and Photocatalytic Mechanism. The $(iso\text{-}BA)_2PbI_4$, $(BA)_2PbI_4$, $(PEA)_2PbI_4$, and $(R/S\text{-}MBA)_2PbI_4$ are utilized to photodegrade organic dyes, and $(iso\text{-}BA)_2PbI_4$ was involved in the capture experiments of the sacrificial reagent to elucidate the photocatalytic mechanism. Four sacrificial species including EDTA, IPA, $AgNO_3$, and p-BQ were employed to capture the photoexcited hole (h^+), hydroxyl radical ($^\bullet OH$), electron (e^-), and superoxide radicals ($^\bullet O_2^-$), respectively. As shown in Figure 5a, the photodegradation rates of MO by $(iso\text{-}BA)_2PbI_4$ did not change when EDTA, isopropanol, and $AgNO_3$ were introduced, indicating that h^+, $^\bullet OH$, and e^- are not the active species in the photocatalytic reaction. When p-benzoquinone was presented, however, the photodegradation rate of MO was significantly suppressed compared with the one without sacrificial agents, confirming that superoxide radicals ($^\bullet O_2^-$) are the reactive active species in the photodegradation process of $(iso\text{-}BA)_2PbI_4$. Additionally, the existence of superoxide radical species ($^\bullet O_2^-$) was indicated by the ESR spectroscopy (Figure S22), in which the ESR spectra of $(iso\text{-}BA)_2PbI_4$ were taken after 1 and 5 min of irradiation of visible light. As revealed in Figure 5b, no ESR signals can be observed without light irradiation, whereas strong ESR signals of superoxide radical species in the reaction solution were detected once exposed to the irradiation of visible light.[54,55] To sum up, the active substance of $(iso\text{-}BA)_2PbI_4$ in the photocatalytic reaction was found to be superoxide radicals.

Besides the high photoactivity, the $(iso\text{-}BA)_2PbI_4$ catalyst also exhibited excellent durability during the photocatalytic reaction, which was very important for the application in practice. Therefore, the reusability of the resulting $(iso\text{-}BA)_2PbI_4$ is inspected by cyclic photodegradation experiments. To be specific, the sample is stirred with the target dye (MO) for 30 min in the dark and then irradiated with a halogen cold light source for 10 min as one cycle. In Figures 5c and S23, $(iso\text{-}BA)_2PbI_4$ exhibits excellent stability within 10 cycles. Then, the degradation rate dropped to 78.10% after 15 cycles and 45.74% after 20 cycles. Meanwhile, the crystal structure and multilayer morphologies were maintained well after 20 cycles, confirmed by the XRD pattern in Figure S24a and the FESEM image in Figure S25. The diffraction peaks of the perovskite samples that underwent multiple cycles exhibit a similar pattern (Figure S24a) to the one before cyclic photodegradation, whereas the crystallinity is not excellent. As observed in Figure S24b, the PL absorption wavelength shifts to blue as the number of cycles increases, which could be attributed to the higher photon energy corresponding to the increased band gap as well as the shortened absorption wavelength that results in a blue shift. As for the UV−vis absorption spectra (Figure S24c), there was no significant difference between the samples that participated in cycles 20 and 0. And the multilayer morphology of the sample was maintained well before and after the testing (Figure S25). Furthermore, in order to analyze and confirm the absence of secondary products in the catalytic reaction, we performed diffuse reflectance spectroscopy and TEM analysis on the samples before and after the $(iso\text{-}BA)_2PbI_4$-catalyzed MO

https://doi.org/10.1021/acsomega.3c08356
ACS Omega 2024, 9, 3931−3941

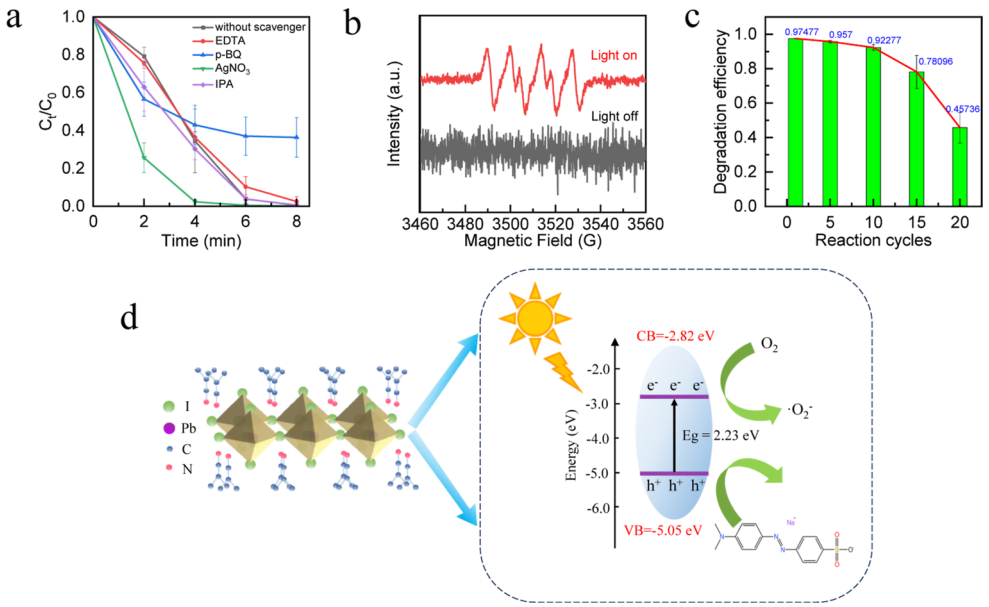

Figure 5. Material stability and photocatalytic mechanism. (a) Effect of the scavenger on photocatalytic degradation of MO by $(iso\text{-}BA)_2PbI_4$ under halogen cold light irradiation. (b) ESR spectra of the superoxide radical species trapped by DMPO over the $(iso\text{-}BA)_2PbI_4$ photocatalyst in the dark or under visible light stimulation for 1 min. (c) Cyclic degradation efficiency of MO by $(iso\text{-}BA)_2PbI_4$. (d) Proposed reaction mechanisms for the removal of organic pollutants with $(iso\text{-}BA)_2PbI_4$.

process. As shown in Figure S26, almost no difference was observed in the spectra of the samples before and after the catalytic process. The two samples before and after photocatalysis were further studied by high-resolution electromagnetic analysis (HRTEM), with the *d*-spacing of pristine $(iso\text{-}BA)_2PbI_4$ calculated to be 0.24 and 0.34 nm, which can be assigned to the (0012) and (008) planes, respectively (Figure S27). After photocatalysis, the lattice spacing remained 0.24 and 0.34 nm, respectively, confirming that the crystallites spacing of (0012) and (008) do not change. Further, no new crystalline phases were found to be generated, indicating that no byproducts were produced.[56−60] Combining the above data with the quality distribution diagram after 20 cycles (Figure S23b), it can be found that $(iso\text{-}BA)_2PbI_4$ has a good structure and photocatalytic stability through the cyclic reactions, which greatly contribute to its prospect applications.

Ultraviolet photoemission spectroscopy was employed to investigate the energy level alignment of a layered heterostructure, which determines the positions of the valence band minimum (VBM) and conduction band maximum (CBM) for $(iso\text{-}BA)_2PbI_4$ (Figure S28). The E_{onset} is 17.23 eV, which is related to secondary electrons. The work function (W_F) of $(iso\text{-}BA)_2PbI_4$ is 3.97 eV, which is relative to 0 eV assigned to the gold standard, defined as the Fermi level (E_F). The difference between E_F and E_{VBM} is 1.08 eV (Figure S28). Based on the band gap (Tauc plot) of $(iso\text{-}BA)_2PbI_4$ (2.23 eV) (Figure S28a), the positions of E_{CBM} (−2.82 eV) and E_{VBM} (−5.05 eV) were determined. Accordingly, the possible band structure and the mechanism of the perovskite on the removal of MO are proposed in Figure 5d. First, the MO is strongly adsorbed by $(iso\text{-}BA)_2PbI_4$ under dark conditions. And the highest energy band (conduction band) of $(iso\text{-}BA)_2PbI_4$ is −2.82 eV, while the lowest energy band (valence band) of $(iso\text{-}BA)_2PbI_4$ is −5.05 eV. When irradiated by the visible light, electron transition occurs immediately and photogenerated electron−hole (e^-−h^+) pairs are produced. Electrons (e^-) can jump from the VB to the CB, leaving holes in the VB. Therefore, the O_2 molecule is photoreduced by electrons to produce superoxide radicals ($^{\bullet}O_2^-$), and the process is illustrated as

$$e^- + O_2 \rightarrow {}^{\bullet}O_2^-$$

Meanwhile, the photoexcited h^+ as active species would interact with the MO molecules to degrade the organic dye directly.[61,62]

4. CONCLUSIONS

Taking $(iso\text{-}BA)_2PbI_4$ as an example, two systems that can stabilize two-dimensional OIHPs are discovered, that is, the original solution with pH 1−8 and the filtrate with pH 1−8. The reason for the superior stability of the 2D halide perovskite was elucidated by characterizations of XRD, PL spectroscopy, UV−vis spectroscopy, XPS, and electrochemical tests. And the photocatalytic property was studied by photocatalytic degradation of organic dyes (MO, SRB, CR, and DB19). The results showed that $(iso\text{-}BA)_2PbI_4$ degraded methyl oranges up to 99% within 10 min with good recoverability, and the mechanism of photocatalytic degradation was proposed according to the result of radical capture experiments and ESR tests. Finally, we investigated the effect of organo-amine ligands in 2D OIHPs on the catalytic performance. It was found that chiral perovskite $(R/S\text{-}MBA)_2PbI_4$ can efficiently degrade MO within 5 min, which can be regarded as one of the fastest catalysts for degradation of MO dye so far. This discovery expands the possibility that 2D OIHPs can be applied in photocatalytic chemistry, possessing significant implication for future exploration on asymmetric catalysis.

■ ASSOCIATED CONTENT

Supporting Information

The Supporting Information is available free of charge at https://pubs.acs.org/doi/10.1021/acsomega.3c08356.

https://doi.org/10.1021/acsomega.3c08356
ACS Omega 2024, 9, 3931−3941

Optical photographs of $(iso\text{-}BA)_2PbI_4$ presented in different solutions, CV spectra of $(iso\text{-}BA)_2PbI_4$ of pH = 1−8, CV spectra of $(iso\text{-}BA)_2PbI_4$ at different pH values, optical photographs of $(PEA)_2PbI_4$ presented in the solutions of pH = 1−14. XRD patterns and UV−vis and PL spectra of $(PEA)_2PbI_4$ UV−vis absorption spectra of $(iso\text{-}BA)_2PbI_4$ on the degradation of methyl orange (30 mg/L) under different conditions, and ESR spectra of $(iso\text{-}BA)_2PbI_4$ kept in the dark and exposed to visible light (PDF)

AUTHOR INFORMATION

Corresponding Author

Jun Wang − *Department of Chemistry, College of Sciences, Northeastern University, Shenyang 110819, P. R. China;* orcid.org/0000-0002-6619-2346; Email: wangjun12@mail.neu.edu.cn

Authors

Mengke Wang − *Department of Chemistry, College of Sciences, Northeastern University, Shenyang 110819, P. R. China*

Xi Zhang − *Department of Chemistry, College of Sciences, Northeastern University, Shenyang 110819, P. R. China*

Lei Liu − *Department of Chemistry, College of Sciences, Northeastern University, Shenyang 110819, P. R. China*

Xiaoyu Zhang − *Department of Chemistry, College of Sciences, Northeastern University, Shenyang 110819, P. R. China*

Jiahe Yan − *Department of Chemistry, College of Sciences, Northeastern University, Shenyang 110819, P. R. China*

Weihua Jin − *Department of Chemistry, College of Sciences, Northeastern University, Shenyang 110819, P. R. China*

Peng Zhang − *Department of Chemistry, College of Sciences, Northeastern University, Shenyang 110819, P. R. China*

Complete contact information is available at: https://pubs.acs.org/10.1021/acsomega.3c08356

Author Contributions

M.W. and X.Z. are the primary writers of the manuscript. M.W. and X.Z. explored and discovered two systems in which two-dimensional OIHPs $(iso\text{-}BA)_2PI_4$ stably existed and characterized it and analyzed the data. M.W. designed photocatalytic experiments on the basis of stability. L.L. carried out photocatalytic degradation experiments of perovskites on different dyes. X.Y.Z. carried out electrochemical experiments and analysis of perovskites stabilized on the basis of their presence at different pH values. W.J. designed and performed electrochemical impedance analysis and electron microscopy imaging of different perovskites. M.W. and J.Y. designed and performed the PL spectroscopy and data analysis. P.Z. was responsible for the review of the whole project. J.W. supervised the execution and editing of the whole project.

Notes

The authors declare no competing financial interest.

ACKNOWLEDGMENTS

W.J. acknowledges support from the National Natural Science Foundation of China (no. 62204032), the Natural Science Foundation of Liaoning Province of China (2021-MS-08), and the Fundamental Research Funds for the Central Universities, NEU (N2305013). We thank the Testing Center of Northeastern University for the support in PL and XRD tests.

ABBREVIATIONS

OIHPs, organic−inorganic hybrid perovskites; HPPs, halide perovskite photocatalysts; IHPQDs, inorganic halide perovskite quantum dots; IHPCQDs, inorganic halide perovskite carbon quantum dots; CQDs, carbon quantum dots; PQDs, perovskite carbon quantum dots; MO, methyl orange; CR, congo red; DB19, direct black 19; SRB, sulforhodamine-B

REFERENCES

(1) Chen, S.; Yin, H.; Liu, P.; Wang, Y.; Zhao, H. Stabilization and Performance Enhancement Strategies for Halide Perovskite Photocatalysts. *Adv. Mater.* **2023**, *35* (6), No. e2203836.

(2) Juntrapirom, S.; Tantraviwat, D.; Suntalelat, S.; Thongsook, O.; Phanichphant, S.; Inceesungvorn, B. Visible light photocatalytic performance and mechanism of highly efficient SnS/BiOI heterojunction. *J. Colloid Interface Sci.* **2017**, *504*, 711−720.

(3) Gao, P.; Liu, J.; Sun, D. D.; Ng, W. Graphene oxide-CdS composite with high photocatalytic degradation and disinfection activities under visible light irradiation. *J. Hazard. Mater.* **2013**, *250*−*251*, 412−420.

(4) Li, Y.; Zhao, H.; Yang, M. TiO_2 nanoparticles supported on PMMA nanofibers for photocatalytic degradation of methyl orange. *J. Colloid Interface Sci.* **2017**, *508*, 500−507.

(5) Nguyen, C. H.; Fu, C.-C.; Juang, R.-S. Degradation of methylene blue and methyl orange by palladium-doped TiO_2 photocatalysis for water reuse: Efficiency and degradation pathways. *J. Cleaner Prod.* **2018**, *202*, 413−427.

(6) Cheng, P.; Han, K.; Chen, J. Recent Advances in Lead-Free Halide Perovskites for Photocatalysis. *ACS Mater. Lett.* **2023**, *5* (1), 60−78.

(7) Wang, H.; Zhang, X.; Ma, Y.; Wang, M.; Wang, J. A Universal Approach for Potassium-Passivated 2D Perovskites. *Sol. RRL* **2022**, *6* (6), 2101019.

(8) Grancini, G.; Nazeeruddin, M. K. Dimensional tailoring of hybrid perovskites for photovoltaics. *Nat. Rev. Mater.* **2019**, *4* (1), 4−22.

(9) Sun, H.; Tian, W.; Wang, X.; Deng, K.; Xiong, J.; Li, L. In Situ Formed Gradient Bandgap-Tunable Perovskite for Ultrahigh-Speed Color/Spectrum-Sensitive Photodetectors via Electron-Donor Control. *Adv. Mater.* **2020**, *32* (14), No. e1908108.

(10) Wehrenfennig, C.; Eperon, G. E.; Johnston, M. B.; Snaith, H. J.; Herz, L. M. High charge carrier mobilities and lifetimes in organolead trihalide perovskites. *Adv. Mater.* **2014**, *26* (10), 1584−1589.

(11) Liu, K.; Jiang, Y.; Jiang, Y.; Guo, Y.; Liu, Y.; Nakamura, E. Chemical Formation and Multiple Applications of Organic-Inorganic Hybrid Perovskite Materials. *J. Am. Chem. Soc.* **2019**, *141* (4), 1406−1414.

(12) Zhang, C.; Wang, B.; Li, W.; Huang, S.; Kong, L.; Li, Z.; Li, L. Conversion of invisible metal-organic frameworks to luminescent perovskite nanocrystals for confidential information encryption and decryption. *Nat. Commun.* **2017**, *8* (1), 1138.

(13) Zhang, H.; Li, W.; Essman, J.; Quarti, C.; Metcalf, I.; Chiang, W.-Y.; Sidhik, S.; Hou, J.; Fehr, A.; Attar, A.; Lin, M.-F.; Britz, A.; Shen, X.; Link, S.; Wang, X.; Bergmann, U.; Kanatzidis, M. G.; Katan, C.; Even, J.; Blancon, J.-C.; Mohite, A. D. Ultrafast relaxation of lattice distortion in two-dimensional perovskites. *Nat. Phys.* **2023**, *19* (4), 545−550.

(14) Wang, Q.; Hisatomi, T.; Jia, Q.; Tokudome, H.; Zhong, M.; Wang, C.; Pan, Z.; Takata, T.; Nakabayashi, M.; Shibata, N.; Li, Y.; Sharp, I. D.; Kudo, A.; Yamada, T.; Domen, K. Scalable water splitting on particulate photocatalyst sheets with a solar-to-hydrogen energy conversion efficiency exceeding 1%. *Nat. Mater.* **2016**, *15* (6), 611−615.

(15) Tsai, H.; Nie, W.; Blancon, J. C.; Stoumpos, C. C.; Asadpour, R.; Harutyunyan, B.; Neukirch, A. J.; Verduzco, R.; Crochet, J. J.; Tretiak, S.; Pedesseau, L.; Even, J.; Alam, M. A.; Gupta, G.; Lou, J.; Ajayan, P. M.; Bedzyk, M. J.; Kanatzidis, M. G.; et al. High-efficiency

two-dimensional Ruddlesden-Popper perovskite solar cells. *Nature* **2016**, *536* (7616), 312−316.
(16) Zhang, F.; Lu, H.; Tong, J.; Berry, J. J.; Beard, M. C.; Zhu, K. Advances in two-dimensional organic-inorganic hybrid perovskites. *Energy Environ. Sci.* **2020**, *13* (4), 1154−1186.
(17) Zhou, N.; Shen, Y.; Li, L.; Tan, S.; Liu, N.; Zheng, G.; Chen, Q.; Zhou, H. Exploration of Crystallization Kinetics in Quasi Two-Dimensional Perovskite and High Performance Solar Cells. *J. Am. Chem. Soc.* **2018**, *140* (1), 459−465.
(18) Hu, J.; Yan, L.; You, W. Two-Dimensional Organic-Inorganic Hybrid Perovskites: A New Platform for Optoelectronic Applications. *Adv. Mater.* **2018**, *30* (48), No. e1802041.
(19) Stoumpos, C. C.; Soe, C. M. M.; Tsai, H.; Nie, W.; Blancon, J.-C.; Cao, D. H.; Liu, F.; Traoré, B.; Katan, C.; Even, J.; Mohite, A. D.; Kanatzidis, M. G. High Members of the 2D Ruddlesden-Popper Halide Perovskites: Synthesis, Optical Properties, and Solar Cells of $(CH_3(CH_2)_3NH_3)_2(CH_3NH_3)_4Pb_5I_{16}$. *Chem* **2017**, *2* (3), 427−440.
(20) Saparov, B.; Mitzi, D. B. Organic-Inorganic Perovskites: Structural Versatility for Functional Materials Design. *Chem. Rev.* **2016**, *116* (7), 4558−4596.
(21) Chen, Y.; Sun, Y.; Peng, J.; Tang, J.; Zheng, K.; Liang, Z. 2D Ruddlesden-Popper Perovskites for Optoelectronics. *Adv. Mater.* **2018**, *30* (2), 1703487.
(22) Cao, D. H.; Stoumpos, C. C.; Farha, O. K.; Hupp, J. T.; Kanatzidis, M. G. 2D Homologous Perovskites as Light-Absorbing Materials for Solar Cell Applications. *J. Am. Chem. Soc.* **2015**, *137* (24), 7843−7850.
(23) Huang, H.; Polavarapu, L.; Sichert, J. A.; Susha, A. S.; Urban, A. S.; Rogach, A. L. Colloidal lead halide perovskite nanocrystals: synthesis, optical properties and applications. *NPG Asia Mater.* **2016**, *8* (11), No. e328.
(24) Li, X.; Wu, Y.; Zhang, S.; Cai, B.; Gu, Y.; Song, J.; Zeng, H. $CsPbX_3$Quantum Dots for Lighting and Displays: Room-Temperature Synthesis, Photoluminescence Superiorities, Underlying Origins and White Light-Emitting Diodes. *Adv. Funct. Mater.* **2016**, *26* (15), 2435−2445.
(25) Protesescu, L.; Yakunin, S.; Bodnarchuk, M. I.; Krieg, F.; Caputo, R.; Hendon, C. H.; Yang, R. X.; Walsh, A.; Kovalenko, M. V. Nanocrystals of Cesium Lead Halide Perovskites ($CsPbX_3$, X = Cl, Br, and I): Novel Optoelectronic Materials Showing Bright Emission with Wide Color Gamut. *Nano Lett.* **2015**, *15* (6), 3692−3696.
(26) Wheeler, L. M.; Sanehira, E. M.; Marshall, A. R.; Schulz, P.; Suri, M.; Anderson, N. C.; Christians, J. A.; Nordlund, D.; Sokaras, D.; Kroll, T.; Harvey, S. P.; Berry, J. J.; Lin, L. Y.; Luther, J. M. Targeted Ligand-Exchange Chemistry on Cesium Lead Halide Perovskite Quantum Dots for High-Efficiency Photovoltaics. *J. Am. Chem. Soc.* **2018**, *140* (33), 10504−10513.
(27) Yen, M. C.; Lee, C. J.; Liu, K. H.; Peng, Y.; Leng, J.; Chang, T. H.; Chang, C. C.; Tamada, K.; Lee, Y. J. All-inorganic perovskite quantum dot light-emitting memories. *Nat. Commun.* **2021**, *12* (1), 4460.
(28) Wang, Q.; Jin, Z.; Chen, D.; Bai, D.; Bian, H.; Sun, J.; Zhu, G.; Wang, G.; Liu, S. F. μ-Graphene Crosslinked $CsPbI_3$ Quantum Dots for High Efficiency Solar Cells with Much Improved Stability. *Adv. Energy Mater.* **2018**, *8* (22), 1800007.
(29) Ling, X.; Zhou, S.; Yuan, J.; Shi, J.; Qian, Y.; Larson, B. W.; Zhao, Q.; Qin, C.; Li, F.; Shi, G.; Stewart, C.; Hu, J.; Zhang, X.; Luther, J. M.; Duhm, S.; Ma, W. 14.1% $CsPbI_3$ Perovskite Quantum Dot Solar Cells via Cesium Cation Passivation. *Adv. Energy Mater.* **2019**, *9* (28), 1900721.
(30) Wang, S.; Zhao, Q.; Hazarika, A.; Li, S.; Wu, Y.; Zhai, Y.; Chen, X.; Luther, J. M.; Li, G. Thermal tolerance of perovskite quantum dots dependent on A-site cation and surface ligand. *Nat. Commun.* **2023**, *14* (1), 2216.
(31) Ke, W.; Kanatzidis, M. G. Prospects for low-toxicity lead-free perovskite solar cells. *Nat. Commun.* **2019**, *10* (1), 965.
(32) Konstantakou, M.; Stergiopoulos, T. A critical review on tin halide perovskite solar cells. *J. Mater. Chem. A* **2017**, *5* (23), 11518−11549.
(33) Ren, K.; Yue, S.; Li, C.; Fang, Z.; Gasem, K. A. M.; Leszczynski, J.; Qu, S.; Wang, Z.; Fan, M. Metal halide perovskites for photocatalysis applications. *J. Mater. Chem. A* **2022**, *10* (2), 407−429.
(34) Schanze, K. S.; Kamat, P. V.; Yang, P.; Bisquert, J. Progress in Perovskite Photocatalysis. *ACS Energy Lett.* **2020**, *5* (8), 2602−2604.
(35) Yuan, M.; Quan, L. N.; Comin, R.; Walters, G.; Sabatini, R.; Voznyy, O.; Hoogland, S.; Zhao, Y.; Beauregard, E. M.; Kanjanaboos, P.; Lu, Z.; Kim, D. H.; Sargent, E. H. Perovskite energy funnels for efficient light-emitting diodes. *Nat. Nanotechnol.* **2016**, *11* (10), 872−877.
(36) Chen, Z.-Y.; Huang, N.-Y.; Xu, Q. Metal halide perovskite materials in photocatalysis: Design strategies and applications. *Coord. Chem. Rev.* **2023**, *481*, 215031.
(37) Wang, J.; Fang, C.; Ma, J.; Wang, S.; Jin, L.; Li, W.; Li, D. Aqueous Synthesis of Low-Dimensional Lead Halide Perovskites for Room-Temperature Circularly Polarized Light Emission and Detection. *ACS Nano* **2019**, *13* (8), 9473−9481.
(38) Jha, S.; Hasan, M.; Khakurel, N.; Ryan, C. A.; McMullen, R.; Mishra, A.; Malko, A. V.; Zakhidov, A. A.; Slinker, J. D. Electrochemical characterization of halide perovskites: Stability & doping. *Mater. Today Adv.* **2022**, *13*, 100213.
(39) Wang, W.; Liu, X.; Wang, J.; Chen, C.; Yu, J.; Zhao, D.; Tang, W. Versatile Self-Assembled Molecule Enables High-Efficiency Wide-Bandgap Perovskite Solar Cells and Organic Solar Cells. *Adv. Energy Mater.* **2023**, *13* (23), 2300694.
(40) Ning, S.; Zhang, S.; Sun, J.; Li, C.; Zheng, J.; Khalifa, Y. M.; Zhou, S.; Cao, J.; Wu, Y. Ambient Pressure X-ray Photoelectron Spectroscopy Investigation of Thermally Stable Halide Perovskite Solar Cells via Post-Treatment. *ACS Appl. Mater. Interfaces* **2020**, *12* (39), 43705−43713.
(41) Wang, J.; Guo, B.; Zhang, X.; Zhang, Z.; Han, J.; Wu, J. Sonocatalytic degradation of methyl orange in the presence of TiO_2 catalysts and catalytic activity comparison of rutile and anatase. *Ultrason. Sonochem.* **2005**, *12* (5), 331−337.
(42) Xu, B.; Li, Y.; Gao, Y.; Liu, S.; Lv, D.; Zhao, S.; Gao, H.; Yang, G.; Li, N.; Ge, L. Ag-AgI/Bi3O4Cl for efficient visible light photocatalytic degradation of methyl orange: The surface plasmon resonance effect of Ag and mechanism insight. *Appl. Catal., B* **2019**, *246*, 140−148.
(43) Zhou, L.; Lei, J.; Wang, L.; Liu, Y.; Zhang, J. Highly efficient photo-Fenton degradation of methyl orange facilitated by slow light effect and hierarchical porous structure of Fe_2O_3-SiO_2 photonic crystals. *Appl. Catal., B* **2018**, *237*, 1160−1167.
(44) Wei, N.; Cui, H.; Song, Q.; Zhang, L.; Song, X.; Wang, K.; Zhang, Y.; Li, J.; Wen, J.; Tian, J. Ag_2O nanoparticle/TiO_2 nanobelt heterostructures with remarkable photo-response and photocatalytic properties under UV, visible and near-infrared irradiation. *Appl. Catal., B* **2016**, *198*, 83−90.
(45) Bi, C.; Cao, J.; Lina, H.; Wang, Y.; Chen, S. Enhanced photocatalytic activity of $Bi1_2O_{17}C_{l2}$ through loading Pt quantum dots as a highly efficient electron capturer. *Appl. Catal., B* **2016**, *195*, 132−140.
(46) Chen, L.; Yang, S.; Hao, B.; Ruan, J.; Ma, P.-C. Preparation of fiber-based plasmonic photocatalyst and its photocatalytic performance under the visible light. *Appl. Catal., B* **2015**, *166−167*, 287−294.
(47) Zhang, Z.; Liang, Y.; Huang, H.; Liu, X.; Li, Q.; Chen, L.; Xu, D. Stable and Highly Efficient Photocatalysis with Lead-Free Double-Perovskite of $Cs_2AgBiBr_6$. *Angew. Chem., Int. Ed.* **2019**, *58* (22), 7263−7267.
(48) Sha, Y.; Mathew, I.; Cui, Q.; Clay, M.; Gao, F.; Zhang, X. J.; Gu, Z. Rapid degradation of azo dye methyl orange using hollow cobalt nanoparticles. *Chemosphere* **2016**, *144*, 1530−1535.
(49) Liu, X.; Xing, Z.; Zhang, Y.; Li, Z.; Wu, X.; Tan, S.; Yu, X.; Zhu, Q.; Zhou, W. Fabrication of 3D flower-like black N-TiO_2-x@MoS_2 for unprecedented-high visible-light-driven photocatalytic performance. *Appl. Catal., B* **2017**, *201*, 119−127.
(50) Hegde, V.; Uthappa, U. T.; Suneetha, M.; Altalhi, T.; Soo Han, S.; Kurkuri, M. D. Functional porous Ce-UiO-66 MOF@Keratin composites for the efficient adsorption of trypan blue dye from

https://doi.org/10.1021/acsomega.3c08356
ACS Omega 2024, 9, 3931−3941

wastewater: A step towards practical implementations. *Chem. Eng. J.* **2023**, *461*, 142103.
(51) Vishal, K.; Aruchamy, K.; Sriram, G.; Ching, Y. C.; Oh, T. H.; Hegde, G.; Ajeya, K. V.; Joshi, S.; Sowriraajan, A.; Jung, H. Y.; Kurkuri, M. Engineering a low-cost diatomite with Zn-Mg-Al Layered triple hydroxide (LTH) adsorbents for the effectual removal of Congo red: Studies on batch adsorption, mechanism, high selectivity, and desorption. *Colloids Surf., A* **2023**, *661*, 130922.
(52) Hu, H.; Chen, M.; Yao, N.; Wu, L.; Zhong, Q.; Song, B.; Cao, M.; Zhang, Q. Highly Stable $CsPbBr_3$ Colloidal Nanocrystal Clusters as Photocatalysts in Polar Solvents. *ACS Appl. Mater. Interfaces* **2021**, *13* (3), 4017−4025.
(53) Bag, M.; Renna, L. A.; Adhikari, R. Y.; Karak, S.; Liu, F.; Lahti, P. M.; Russell, T. P.; Tuominen, M. T.; Venkataraman, D. Kinetics of Ion Transport in Perovskite Active Layers and Its Implications for Active Layer Stability. *J. Am. Chem. Soc.* **2015**, *137* (40), 13130−13137.
(54) Cui, Z.; Wang, W.; Zhao, C.; Chen, C.; Han, M.; Wang, G.; Zhang, Y.; Zhang, H.; Zhao, H. Spontaneous Redox Approach to the Self-Assembly Synthesis of Au/CeO_2 Plasmonic Photocatalysts with Rich Oxygen Vacancies for Selective Photocatalytic Conversion of Alcohols. *ACS Appl. Mater. Interfaces* **2018**, *10* (37), 31394−31403.
(55) Huo, Y.; Zhang, J.; Miao, M.; Jin, Y. Solvothermal synthesis of flower-like BiOBr microspheres with highly visible-light photocatalytic performances. *Appl. Catal., B* **2012**, *111*−*112*, 334−341.
(56) Duong, T.; Pham, H.; Kho, T. C.; Phang, P.; Fong, K. C.; Yan, D.; Yin, Y.; Peng, J.; Mahmud, M. A.; Gharibzadeh, S.; Nejand, B. A.; Hossain, I. M.; Khan, M. R.; Mozaffari, N.; Wu, Y.; Shen, H.; Zheng, J.; Mai, H.; Liang, W.; Samundsett, C.; Stocks, M.; McIntosh, K.; Andersson, G. G.; Lemmer, U.; Richards, B. S.; Paetzold, U. W.; Ho-Ballie, A.; Liu, Y.; Macdonald, D.; Blakers, A.; Wong-Leung, J.; White, T.; Weber, K.; Catchpole, K. High Efficiency Perovskite-Silicon Tandem Solar Cells: Effect of Surface Coating versus Bulk Incorporation of 2D Perovskite. *Adv. Energy Mater.* **2020**, *10* (32), 1903553.
(57) Li, Y.; Ding, L. Single-crystal perovskite devices. *Sci. Bull.* **2021**, *66* (3), 214−218.
(58) Liu, Y.; Zhang, Y.; Yang, Z.; Ye, H.; Feng, J.; Xu, Z.; Zhang, X.; Munir, R.; Liu, J.; Zuo, P.; Li, Q.; Hu, M.; Meng, L.; Wang, K.; Smilgies, D.-M.; Zhao, G.; Xu, H.; Yang, Z.; Amassian, A.; Li, J.; Zhao, K.; Liu, S. Multi-inch single-crystalline perovskite membrane for high-detectivity flexible photosensors. *Nat. Commun.* **2018**, *9* (1), 5302.
(59) Lu, D.; Lv, G.; Xu, Z.; Dong, Y.; Ji, X.; Liu, Y. Thiophene-Based Two-Dimensional Dion-Jacobson Perovskite Solar Cells with over 15% Efficiency. *J. Am. Chem. Soc.* **2020**, *142* (25), 11114−11122.
(60) Ye, L.; Guo, P.; Su, J.; Zhang, K.; Liu, C.; Yang, P.; Zhao, W.; Zhao, P.; Liu, Z.; Chang, J.; Ye, Q.; Wang, H. Managing Secondary Phase Lead Iodide in Hybrid Perovskites via Surface Reconstruction for High-Performance Perovskite Solar Cells with Robust Environmental Stability. *Angew. Chem., Int. Ed.* **2023**, *62* (18), No. e202300678.
(61) Tian, J.; Yan, T.; Qiao, Z.; Wang, L.; Li, W.; You, J.; Huang, B. Anion-exchange synthesis of Ag_2S/Ag_3PO_4 core/shell composites with enhanced visible and NIR light photocatalytic performance and the photocatalytic mechanisms. *Appl. Catal., B* **2017**, *209*, 566−578.
(62) Ge, M. Photodegradation of rhodamine B and methyl orange by Ag_3PO_4 catalyst under visible light irradiation. *Chin. J. Catal.* **2014**, *35* (8), 1410−1417.

https://doi.org/10.1021/acsomega.3c08356
ACS Omega 2024, 9, 3931−3941